PERGAMON

International Journal of Solids and Structures 38 (2001) 7659–7680

INTERNATIONAL JOURNAL OF SOLIDS and STRUCTURES

www.elsevier.com/locate/ijsolstr

Shock wave-loaded plates

M. Stoffel, R. Schmidt, D. Weichert *

RWTH Aachen, Institut fur Allgemeine Mechanik, Templergraben 64, D-52056 Aachen, Germany

Received 16 November 1999

Abstract

The present paper reports on modeling, numerical simulation, and experimental investigation of plates subjected to impulsive loading. The kinematical hypothesis used for the theoretical description of the transient response includes transverse shear deformations, rotary inertia, and geometrical nonlinear effects. The material modeling accounts for elastic–plastic behavior, isotropic and kinematical hardening, and strain rate sensitivity. The numerical simulation of the transient inelastic vibrations is performed using isoparametric finite elements. Both the Chaboche and the Bodner–Partom viscoplastic constitutive laws are used to trace the evolution of the material characteristics in the framework of a layered shell model. The theoretical and numerical developments are checked by experimental investigations of thin steel plates subjected to shock waves. These experiments are performed in a shock tube with various impact periods and loading histories. The topics addressed in this report include (a) the correlation of experimental and simulated transient inelastic response using the Chaboche and Bodner–Partom models, (b) the sensitivity of the predicted structural response to variations of the material parameters identified on the basis of uniaxial tension tests, (c) the effect of the transverse shear stress distribution on the local evolution of the material behavior and on the global dynamic response, (d) the evolution of deflections, stresses, and plastic zones under blast loading conditions.

Keywords: Plates; Viscoplasticity; Shock tube; Non-linear dynamics; FEM

1. Introduction

Theoretical modeling and numerical simulation of the inelastic dynamic response of structural elements are problems of considerable relevance in the design of engineering structures exposed to severe transient loadings. In literature several approaches are reported on how to investigate the inelastic dynamic behavior of structures subjected to impulsive loading experimentally and to simulate the response numerically based on various constitutive models and structural theories. These papers may be divided into two groups assuming either that the dynamic load is such that at a given time a velocity field is instantaneously imparted to the structure or that the structure is loaded by a pressure pulse of short duration. For full references on the vast literature in this field we refer to monographs like e.g. (Stronge and Yu, 1993; Jones, 1989). The

* Corresponding author. Tel.: +49-241-804-600; fax: +49-241-888-8231.
E-mail address: weichert@iam.rwth-aachen.de (D. Weichert).

0020-7683/01/$ - see front matter
PII: S0020-7683(01)00038-5

present paper discusses exclusively such works in which theoretical predictions of time history responses and/or final structural deformations of impulsively loaded structural elements are compared with experimental data.

Experimental investigations of structures subjected to an instantaneously imparted velocity field are performed by using sheet explosives placed on the structure (see e.g. Florence and Firth, 1965; Florence, 1966; Leech et al., 1968; Wierzbicki and Florence, 1970; Jones and Walters, 1972; Bodner and Symonds, 1979). Pressure pulse loading conditions are usually realized experimentally by shock waves generated by explosives that detonate at some distance from the structure (see e.g. Idczak et al., 1981; Renard and Pennetier, 1996; Pennetier, 1998). An alternative experimental technique for impulsive loading consists of the adaptation of the shock tube principle, well established in experimental supersonic gas dynamics, and allowing either shock or expansion waves. In Gerard (1956) an impact tube is presented in which an expansion wave is used to create a pressure pulse when it impinges on a plate specimen. It appears that the shock tube technique has distinct advantages over test techniques using explosives. One of them is that the front wave is plane, thus yielding a uniformly distributed pressure pulse on plane structural elements. In addition, the pressure history can be measured easily by only one pressure transducer integrated in the specimen mounting ring. This allows for very precise modeling of the transient loading conditions in comparative numerical simulations. In the contrary shock wave fronts generated by detonations of a gaseous mixture (as e.g. in Renard and Pennetier, 1996; Pennetier, 1998) are spherical in free space and lead to a complex time–space evolution of the pressure distribution on plane structural elements. Similarly, front shock waves of cylindrical charges of plastic explosives used in Idczak et al. (1981) do not yield uniformly distributed pressure pulses. As a result an accurate modeling of the history of the impulsive loading in each point of the structure is hardly possible. Such uncertainties of the externally applied forces are also suspected in Witmer et al. (1963) to be one of the reasons for discrepancies between experimentally observed and numerically simulated permanent central deflections of blast-loaded circular aluminum alloy plates. Similarly, the plots of numerically determined permanent deflections versus detonation intensity in Idczak et al. (1981) and Renard and Pennetier (1996) for circular brass and aluminum alloy plates, respectively, show the right tendency but underpredict the experimental results considerably. The difficulties in modeling the time–space evolution of the pressure pulse distribution on structures due to detonations are also reflected in the comparison of the experimentally and numerically determined transient large amplitude vibration response of blast loaded circular aluminum alloy plates in Pennetier (1998) especially in the short time interval prior to the arrival of the plastic zone at the plate center.

As pointed out in Gerard (1956) the planarity of the loading conditions in impact tubes can be even improved if shock waves instead of expansion waves are employed to create a pressure pulse. Shock waves that are not perfectly plane initially can be made plane by using chambers of sufficient length. In the present paper, experiments are performed with an impact tube of that type. By rupturing a diaphragm of a high-pressure chamber a shock wave is created which travels through a low-pressure chamber toward a thin steel plate under investigation. When the shock wave impinges on the plate the pressure time history and the specimen response are measured directly by high frequency response pressure transducers and capacitive displacement sensors, respectively.

Numerical simulation of the inelastic plate response to impulsive loading has been carried out in literature based on a large variety of assumptions concerning the structural behavior and is, therefore, based on numerous structural theories and different constitutive equations. As to the structural hypotheses, the theories adopted range from linear bending theory of plates (e.g. in Wang, 1955), to theories in which only the membrane forces have been considered important, (like e.g. in Idczak et al., 1980, 1981) where membrane shell theories involving different degrees of geometrical nonlinearity for small, moderately large or finite deflections, respectively, are employed. In Florence (1966) experiments on simply supported circular aluminum and steel plates subjected to sheet explosives revealed that due to the deformations becoming large enough to bring membrane forces into play, plates show considerable increase in strength and the

permanent central deflection can be predicted only in a narrow range of deformations by a bending theory. On the other hand, membrane shell theories are adequate only for very large deflections, because the influence of effects associated with the generation of bending states decreases with increasing deformations of the shell. In Batra and Dubey (1971), an improvement on the prediction of the plate response to explosive loading yielding also a very good agreement with the experimental results of Florence (1966) was achieved by accounting for the continuously varying curvature of the deformed surface, hence considering the geometrical nonlinearity with the combined effect of bending moments and membrane forces. Geometrically nonlinear Kirchhoff–Love type shell theory was also employed in Witmer et al. (1963) and Leech et al. (1968) for the simulation of the transient response of plates and shells experimentally investigated under explosive or blast loading conditions. Recently simulation of experimentally observed center deflections of plates subjected to blast loading was performed in Renard and Pennetier (1996) and Pennetier (1998) on the basis of classical von Kármán plate theory and in Pennetier (1998) by using a Kirchhoff–Love type shell theory with nonlinear membrane but linear bending strain-displacement relations. Similar to the structural models, the analysis of the transient response to explosive or blast loading reported in literature is based on a large variety of constitutive models for the simulation of the inelastic material behavior ranging from rigid-perfectly plastic theory to elastic–plastic models including hardening and strain-rate effects. It was shown in Florence and Firth (1965) and Florence (1966) by experiments on impulsively loaded structural elements that the rigid-plastic theory is a reasonable first-order approximation for the prediction of permanent deflections if the plastic deformation or work is large enough. It was concluded that it is reasonable to neglect the elastic deformation or strain energy if the ratio of the kinetic energy input to the elastic strain energy capacity is greater than about 2–3 for beams and about 4 for plates made from aluminum or steel. By correlating predicted and experimental permanent deflections of strain rate insensitive aluminum and strain rate sensitive steel plates it was found in Wierzbicki and Florence (1970) that the effects of strain rate sensitivity are comparable to those of large deflections, and that both are equally responsible for the deflections being below those predicted by the bending theory of rigid-perfectly plastic plates. Elastic, strain-hardening, strain rate sensitive material behavior was employed in Witmer et al. (1963) and Leech et al. (1968) for the simulation of dynamic inelastic plate and shell response to explosive loads. Various other variants have been used in the literature, so e.g. rigid, linear strain hardening material with no strain rate effects in Batra and Dubey (1971), rigid-viscoplastic material with no hardening effects in Idczak et al. (1980, 1981). Different approaches can be also observed concerning the prediction of yield initiation. In structural theories based on the Kirchhoff–Love hypothesis the yield condition is typically considered under plane-stress conditions (e.g. in Witmer et al., 1963; Leech et al., 1968), hence neglecting the effect of transverse shear stresses. In Renard and Pennetier (1996) the plasticity criterion is only applied to terms containing membrane tensions, because the effect of bending on yield is considered small.

The present investigation is aimed at simulating the experimental transient large amplitude oscillations and permanent deflections of steel plates tested in a shock tube, and at predicting local phenomena like the development of stresses, yield initiation, and the spread of plastic zones. To this end none of the above mentioned simplifications concerning the structural and material models, respectively, will be employed. The theoretical and numerical developments are performed by considering elastic–plastic deformations, hardening, strain rate sensitivity, and the combined effect of bending moments, membrane forces and transverse shear forces.

The constitutive equations employed in the present study include the model of Chaboche in its classical form and in an extended version for high strain rates (Chaboche, 1989) as well as the model of Bodner and Partom (1975). The material parameters for the thin steel plates are determined by uniaxial tension tests at different strain rates using identification methods developed in Lindholm et al. (1985) and Chan et al. (1988). For the theoretical modeling a geometrically nonlinear first-order shear deformation (FOSD) theory of layered shells given in Schmidt and Reddy (1988) and Schmidt and Weichert (1989) is used. The numerical developments presented in this paper are based on a finite element code that was developed in

Palmerio et al. (1990), Kreja and Schmidt (1995) and Kreja et al. (1997), extended for transient analysis by employing the central difference method of time integration in Kłosowski and Schmidt (1993, 1994) and for the simulation of viscoplastic material behavior in Kłosowski et al., 1995a,b, 1996, respectively, and adopted recently in Woznica (1996, 1997, 1998), Woznica and Kłosowski (1997) and Kłosowski (1999). Here particular emphasis is focused on refined modeling and numerical simulation of the effect of transverse shear stresses on the predicted inelastic structural response which is particularly important for transient loading conditions with increasing pulse intensity and decreasing pulse duration (see e.g. Jones, 1989). The improvement introduced in the present finite element analysis consists in the employment of a refined modified transverse shear stress distribution (MTSD) for the simulation of the material behavior. Comparative analyses using either the average transverse shear stress distribution of classical FOSD analysis or the refined MTSD show for the latter one better correlation of the experimental and simulated oscillations as well as large quantitative and even qualitative differences in the prediction of local phenomena like yield initiation and plastic strain propagation. Another main goal of the present paper is the comparative numerical analysis of the dynamic plate response based on different constitutive equations. In earlier papers (Kłosowski et al., 1995a,b, 1996; Woznica and Kłosowski, 1997) greater differences were observed between the predicted inelastic responses using the Chaboche and Bodner–Partom models, respectively, which is due to the fact that material parameters had to be adopted from various sources available in literature. Here, based on the identification of material parameters for the plates used in the shock tube experiments, a very good agreement is observed between the numerical simulations based on the Chaboche and the Bodner–Partom models. A special study is devoted to the sensitivity of the predicted vibration response to variations of the experimentally determined material parameters for both models.

First results were published in Stoffel et al. (1998), Stoffel and Weichert (1999); and Weichert and Stoffel (1998). For further results in this context we refer to our papers (Stoffel et al., 1999, 2000; Kłosowski et al., in press; Chroscielewski et al., in press), which include, among others, the study of plates from different materials and the response to repeated loading.

2. Constitutive equations

The shock tube experiments reported in Section 5 of this paper were performed using circular steel plates of 2 mm thickness. The material is classified as St37 according to German standards. The material parameters required for the numerical simulation of the inelastic plate response on the basis of the Chaboche and Bodner–Partom viscoplastic models were determined using steel specimens cut out from the same metal sheets as the plates. Because of the thinness of these specimens only uniaxial tension tests and no compression tests could be performed.

2.1. Chaboche model

The Chaboche law is considered in two different forms, in the classical form and in an extended version for high strain rates (Chaboche, 1989). They are given by the following set of equations:

$$\dot{\boldsymbol{\varepsilon}}^{\boldsymbol{p}} = \frac{3}{2}\dot{p}\frac{\boldsymbol{s}' - \boldsymbol{X}'}{J_2(\boldsymbol{s}' - \boldsymbol{X}')}, \tag{1}$$

$$\dot{p} = \left\langle \frac{\sigma_v}{K} \right\rangle^n \eta, \tag{2}$$

$$\sigma_v = J_2(\boldsymbol{s}' - \boldsymbol{X}') - R - k, \tag{3}$$

$$\dot{\boldsymbol{X}} = \frac{2}{3} a \dot{\boldsymbol{\varepsilon}}^{\boldsymbol{p}} - c \boldsymbol{X} \dot{p}; \quad \dot{R} = b(R_1 - R)\dot{p}, \tag{4}$$

$$\begin{array}{cc} \text{extended form} & \text{classical form} \\ \eta = \mathrm{e}^{\alpha \sigma_v} & \eta = 1 \end{array}. \tag{5}$$

Here $\boldsymbol{\varepsilon}^{\boldsymbol{p}}$, p, $\boldsymbol{s}$, $\boldsymbol{X}$, R, $(\dot{\ })$, $(\ )'$, $J_2(\ )$ denote the Green plastic strain tensor, the invariant of the plastic strain tensor, the second Piola–Kirchhoff stress tensor, the backstress tensor, the isotropic hardening, the derivative with respect to time, the deviatoric part of a tensor and the second invariant of a tensor, respectively. The yield limit k and a, b, c, R_1, n, K are material parameters to be determined by experiments.

2.2. Bodner–Partom model

The law of Bodner–Partom belongs to a class of viscoplastic theories, which does not take a yield surface into account. Therefore each point in the stress space presents a viscoplastic state. The law is expressed by the following equations (see Bodner and Partom, 1975):

$$\dot{\epsilon}_{ij}^{p} = \frac{3}{2} \dot{p} \frac{\boldsymbol{s}'}{J_2(\boldsymbol{s}')}, \tag{6}$$

$$\dot{p} = \frac{2}{\sqrt{3}} D_0 \exp\left[-\frac{1}{2} \left(\frac{R + D}{J_2(\boldsymbol{s}')} \right)^{2n} \frac{n+1}{n} \right], \tag{7}$$

$$D = X_{ij} \frac{\boldsymbol{s}}{J_2(\boldsymbol{s})}, \tag{8}$$

$$\dot{R} = m_1 (R_1 - R) \dot{W}_{\mathrm{p}}, \tag{9}$$

$$\dot{W}_{\mathrm{p}} = \boldsymbol{s} \dot{\boldsymbol{\epsilon}}^{\boldsymbol{p}}, \tag{10}$$

$$\dot{\boldsymbol{X}} = m_2 \left(\frac{3}{2} D_1 \frac{\boldsymbol{s}}{J_2(\boldsymbol{s})} - \boldsymbol{X} \right) \dot{W}_{\mathrm{p}}. \tag{11}$$

Here $R(t = 0) = R_0$ denotes the initial isotropic hardening, W_{p} stands for the plastic work, and m_1, m_2, R_1, D_1, D_0, n, R_0 are material parameters to be identified from tension tests.

3. Shell theory

For the numerical simulation of the transient viscoplastic response a finite element method based on a geometrically nonlinear FOSD shell theory is used. A short summary of the used kinematics is given below, derivations of this shell model are presented in Schmidt and Reddy (1988) and Schmidt and Weichert (1989) in detail.

In the framework of the FOSD theory the tangential and normal displacements in the shell space referred to the base vectors of the midsurface, v_α and v_3, are expressed by

$$v_\alpha = \overset{0}{v}_\alpha + \theta \overset{1}{v}_\alpha; \qquad v_3 = \overset{0}{v}_3, \ \ \alpha = 1, 2, \tag{12}$$

where $\overset{0}{v}_\alpha$, $\overset{0}{v}_3$ are the tangential and normal displacements and $\overset{1}{v}_\alpha$ the rotations at the midsurface, respectively, while θ denotes the normal coordinate. Assuming small strains and moderate rotations the general Green–Lagrange strain tensor in the shell space can be expressed by

$$\varepsilon_{\alpha\beta} = \overset{0}{\varepsilon}_{\alpha\beta} + \theta\overset{1}{\varepsilon}_{\alpha\beta} + \theta^2\overset{2}{\varepsilon}_{\alpha\beta}, \tag{13}$$

$$\varepsilon_{\alpha 3} = \overset{0}{\varepsilon}_{\alpha 3} + \theta\overset{1}{\varepsilon}_{\alpha 3}, \tag{14}$$

$$\varepsilon_{33} = \overset{0}{\varepsilon}_{33}, \tag{15}$$

with

$$\overset{0}{\varepsilon}_{\alpha\beta} = \overset{0}{\theta}_{\alpha\beta} + \tfrac{1}{2}\overset{0}{\varphi}_\alpha\overset{0}{\varphi}_\beta, \tag{16}$$

$$\overset{1}{\varepsilon}_{\alpha\beta} = \tfrac{1}{2}\left(\overset{1}{v}_\alpha|_\beta + \overset{1}{v}_\beta|_\alpha\right) - \tfrac{1}{2}\left(b^\lambda_\alpha\overset{0}{\varphi}_{\lambda\beta} + b^\lambda_\beta\overset{0}{\varphi}_{\lambda\alpha}\right) + \tfrac{1}{2}\left(\overset{0}{\varphi}_\alpha b^\lambda_\beta\overset{1}{v}_\lambda + \overset{0}{\varphi}_\beta b^\lambda_\alpha\overset{1}{v}_\lambda\right), \tag{17}$$

$$\overset{2}{\varepsilon}_{\alpha\beta} = -\tfrac{1}{2}\left(b^\lambda_\alpha\overset{1}{v}_\lambda|_\beta + b^\lambda_\beta\overset{1}{v}_\lambda|_\alpha\right) + \tfrac{1}{2}b^\lambda_\alpha b^\kappa_\beta\overset{1}{v}_\lambda\overset{1}{v}_\kappa, \tag{18}$$

$$\overset{0}{\varepsilon}_{\alpha 3} = \tfrac{1}{2}\left(\overset{0}{\varphi}_\alpha + \overset{1}{v}_\alpha\right) + \tfrac{1}{2}\overset{1}{v}^\lambda\overset{0}{\varphi}_{\lambda\alpha}, \tag{19}$$

$$\overset{1}{\varepsilon}_{\alpha 3} = \tfrac{1}{2}\overset{1}{v}^\lambda\overset{1}{v}_\lambda|_\alpha, \qquad \overset{0}{\varepsilon}_{33} = 0. \tag{20}$$

Here the abbreviations

$$\overset{0}{\theta}_{\alpha\beta} = \tfrac{1}{2}\left(\overset{0}{v}_\alpha|_\beta + \overset{0}{v}_\beta|_\alpha\right) - b_{\alpha\beta}\overset{0}{v}_3, \qquad \overset{0}{\varphi}_{\alpha\beta} = \overset{0}{v}_\alpha|_\beta - b_{\alpha\beta}\overset{0}{v}_3, \tag{21}$$

$$\overset{0}{\varphi}_\alpha = \overset{0}{v}_{3,\alpha} + b^\lambda_\alpha\overset{0}{v}_\lambda, \tag{22}$$

have been used, where $b_{\alpha\beta}$ and b^λ_α denote the covariant and mixed components of the curvature tensor, while $(.)|_\alpha$ denotes covariant differentiation with respect to the coordinate θ^α. Here and in the following the Einstein summation convention has been adopted with Greek indices ranging from 1 to 2 and Latin indices ranging from 1 to 3.

For the derivation of the equations of motion the principle of virtual work is used in the form

$$\int_{\mathscr{V}}\left[s^{ij}\delta\varepsilon_{ij}(\boldsymbol{V}) - \rho(F^i - A^i)\delta V_i\right]\mathrm{d}\mathscr{V} - \int_{\mathscr{A}}({}^*s^i + D^i)\delta V_i\,\mathrm{d}\mathscr{A} = 0. \tag{23}$$

Here s^{ij} are the components of the second Piola–Kirchhoff stress tensor, V_i are the components of the displacement vector, ρ denotes the mass density per unit volume of the undeformed body, F^i and A^i are the components of the body force and acceleration vector, ${}^*s^i$ and D^i denote the components of the prescribed external stress vector and of the damping force vector (per unit area of the undeformed bounding surface $\mathscr{A}$) and $\mathscr{V}$ is the volume of the body. For viscous damping the components of the damping force vector are proportional to the velocity, i.e. they are given by $D^i = -D^{ij}\dot{V}_j$ with D^{ij} denoting the components of the damping tensor.

If transient viscoplastic analysis is considered, it is necessary to use a layered shell model which permits to trace the evolution of the material law separately in each layer. The transformation of the 3D principle of virtual work (23) into a 2D formulation using Eqs. (12)–(15) yields

$$\int_{\mathscr{M}} \sum_{k=1}^{\ell} \left\{ \sum_{n=0}^{2} \overset{n}{L}{}^{\alpha\beta}_{(k)} \delta \overset{n}{\varepsilon}_{\alpha\beta} + 2 \sum_{n=0}^{1} \overset{n}{L}{}^{\alpha 3}_{(k)} \delta \overset{n}{\varepsilon}_{\alpha 3} - \sum_{n=0}^{1} \left[\left(\overset{n}{F}{}^{\alpha}_{(k)} - \overset{n}{I}{}^{\alpha}_{(k)} - \overset{n}{D}{}^{\alpha}_{(k)} + \overset{n}{p}{}^{\alpha} \right) \delta \overset{n}{v}_{\alpha} \right] \right.$$
$$\left. - \left(\overset{0}{F}{}^{3}_{(k)} - \overset{0}{I}{}^{3}_{(k)} - \overset{0}{D}{}^{3}_{(k)} + \overset{0}{p}{}^{3} \right) \delta \overset{0}{v}_{3} \right\} \mathrm{d}\mathscr{M} - \int_{\mathscr{L}} \sum_{k=1}^{\ell} \left\{ \sum_{n=0}^{1} \left[{}^{*}\overset{n}{L}{}^{\alpha\beta}_{(k)} v_{\alpha} v_{\beta} \delta \overset{n}{v}_{\nu} + {}^{*}\overset{n}{L}{}^{\alpha\beta}_{(k)} t_{\alpha} v_{\beta} \delta \overset{0}{v}_{t} \right] + {}^{*}\overset{0}{L}{}^{3\beta}_{(k)} v_{\beta} \delta \overset{0}{v}_{3} \right\} \mathrm{d}\mathscr{L} = 0. \tag{24}$$

Here $\mathscr{M}$ and $\mathscr{L}$ are the reference surface and the boundary line, v_α, t_α denote the components of the unit outward normal and tangent vectors of $\mathscr{L}$, ℓ denotes the number of layers used in the model and k is the layer identificator. Furthermore, we have used the following definitions (see Librescu and Schmidt, 1988; Kłosowski and Schmidt, 1996) for

(a) the nth order stress couples

$$\overset{n}{L}{}^{\alpha\beta}_{(k)} = \int_{z_k}^{z_{k+1}} c_{(k)} \overset{\lambda\beta}{s}{}_{(k)} \theta^n \, \mathrm{d}\theta, \qquad \overset{n}{L}{}^{\alpha 3}_{(k)} = \int_{z_k}^{z_{k+1}} c_{(k)} \overset{\alpha 3}{s}{}_{(k)} \theta^n \, \mathrm{d}\theta, \tag{25}$$

(b) the nth order body couples

$$\overset{n}{F}{}^{\alpha}_{(k)} = \int_{z_k}^{z_{k+1}} \rho c_{(k)} c^{\alpha}_{(k)\beta} F^{\beta} \theta^n \, \mathrm{d}\theta, \qquad \overset{0}{F}{}^{3}_{(k)} = \int_{z_k}^{z_{k+1}} \rho c_{(k)} F^{3} \, \mathrm{d}\theta, \tag{26}$$

(c) the nth order inertia couples

$$\overset{n}{I}{}^{\alpha}_{(k)} = \sum_{q=0}^{1} \overset{q+n}{i}{}_{(k)} \overset{q}{\ddot{v}}{}^{\alpha}, \qquad \overset{0}{I}{}^{3}_{(k)} = \overset{0}{i}{}_{(k)} \overset{0}{\ddot{v}}{}^{3}, \tag{27}$$

where

$$\overset{m}{i}{}_{(k)} = \int_{z_k}^{z_{k+1}} \rho c_{(k)} \theta^m \, \mathrm{d}\theta, \tag{28}$$

(d) the nth order damping couples

$$\overset{n}{D}{}^{\alpha}_{(k)} = -\sum_{q=0}^{1} \left({}^{+}\overset{q+n}{d}{}^{\alpha\beta} + {}^{-}\overset{q+n}{d}{}^{\alpha\beta} \right) \overset{q}{\dot{v}}_{\beta}, \qquad \overset{0}{D}{}^{3}_{(k)} = -\left({}^{+}\overset{0}{d}{}^{33} + {}^{-}\overset{0}{d}{}^{33} \right) \overset{0}{\dot{v}}_{3} \tag{29}$$

with

$${}^{\pm}\overset{n}{d}{}^{\alpha\beta} = \left[c c^{\alpha}_{\lambda} c^{\beta}_{\gamma} D^{\lambda\gamma} \left(\theta^3 \right)^n \right] \Big|_{\pm h/2}, \qquad {}^{\pm}\overset{0}{d}{}^{33} = \left[c D^{33} \right] \Big|_{\pm h/2}, \tag{30}$$

(e) the nth order couples of the surface loads on the upper and lower surfaces

$$\overset{n}{p}{}^{\alpha} = \left[c c^{\alpha *}_{\beta} t^{3\beta} \theta^m \right] \Big|_{-h/2}^{h/2}, \qquad \overset{n}{p}{}^{3} = \left[c^{*} t^{33} \right] \Big|_{-h/2}^{h/2}, \tag{31}$$

(f) the nth order couples of the prescribed boundary loads

$${}^{*}\overset{n}{L}{}^{\alpha\beta}_{(k)} = \int_{z_k}^{z_{k+1}} c_{(k)} c^{\alpha}_{(k)\lambda} \, {}^{*}t^{\beta\lambda} \theta^n \, \mathrm{d}\theta, \qquad {}^{*}\overset{0}{L}{}^{3\beta}_{(k)} = \int_{z_k}^{z_{k+1}} c_{(k)} \, {}^{*}t^{\beta 3} \, \mathrm{d}\theta. \tag{32}$$

Here c^{α}_{λ} and c are the components of the shifter tensor and its determinant, respectively, ${}^{*}t^{ij}$ denotes the prescribed components of the first Piola–Kirchhoff stress tensor while z_k and z_{k+1} are the coordinates of the lower and upper surfaces of the kth layer in direction of θ.

The principle of virtual work (24) along with the strain–displacement relations (13)–(22) and the constitutive equations of Section 2 represents the theoretical framework for the analysis of the dynamic response of viscoplastic structures adopted in this paper.

Additional considerations have been made concerning the distribution of transverse shear stresses through the thickness obtained from the above FOSD model and its influence on the predicted transient response via the inelastic constitutive equations. It is well known that the effect of transverse shear forces on the static response of thin metallic structures is small. It has been shown, however, (e.g. in Jones, 1989) that transverse shear forces are potentially more important for transient loading conditions, in particular in the early stages of motion, and that their influence on the inelastic response grows with increasing pulse intensity and decreasing pulse duration. Due to the kinematical hypothesis of the FOSD theory expressed by Eq. (12) the effects of transverse shear stresses are included in the present analysis. Also in the constitutive equations the influence of the transverse shear stresses, e.g. on the deviatoric part and the second invariant of the stress tensor are fully taken into account. However, the distribution of the transverse shear stresses through the thickness resulting from the FOSD hypothesis equation (12) represents the effect of the transverse shear forces only in an average sense. As a consequence, in the elastic range the transverse shear stresses in the upper and lower zones of the plate – which are in fact zero for zero tangential loading – are predicted too high, while the transverse shear stresses near the midsurface are predicted too low. Consequently, using the transverse shear stress distribution obtained by means of the FOSD theory in the yield condition predicts yield initiation in the upper and lower zones too early and, vice versa, near the midsurface too late. In this context it has been pointed out (e.g. in Jones, 1989), that the effect of shear on yield during dynamic deformation is often significant. Therefore, in the present paper a more realistic transverse shear stress distribution through the thickness is proposed which allows to simulate the yield initiation more precisely than the transverse shear stress distribution obtained from the FOSD theory.

The approach adopted here consists of a redistribution of the average transverse shear stress $s_m^{\alpha 3}$ obtained on the basis of FOSD theory into a parabolic function $s^{\alpha 3}(\theta)$ in such a way that

$$\int_{-h/2}^{h/2} s^{\alpha 3}(\theta)\,\mathrm{d}\theta = s_m^{\alpha 3} h \tag{33}$$

and the zero shear stress loading conditions at the upper and lower surfaces are satisfied, i.e.

$$s^{\alpha 3}\left(\theta = \frac{h}{2}\right) = 0, \qquad s^{\alpha 3}\left(\theta = -\frac{h}{2}\right) = 0. \tag{34}$$

This results in

$$s^{\alpha 3}(\theta) = \kappa s_m^{\alpha 3}, \qquad \kappa = \frac{3}{2}\left(1 - \frac{4\theta^2}{h^2}\right). \tag{35}$$

Fig. 1 shows the 10 layer model used for the numerical simulations with the transverse shear stress distribution according to Eq. (35). The transverse shear stresses for each layer are calculated at the midsurface of the respective layer and assumed constant over the layer thickness.

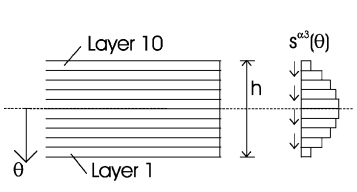

layer	θ	κ
1	$\frac{9}{20}h$	0.285
2	$\frac{7}{20}h$	0.765
3	$\frac{5}{20}h$	1.125
4	$\frac{3}{20}h$	1.365
5	$\frac{1}{20}h$	1.485

Fig. 1. Modified transverse shear stress distribution.

Comparative analysis in Section 7 using either the FOSD transverse shear stress distribution or the above MTSD in the yield condition reveals that the effect on the prediction of the yield initiation is significant and that the latter one leads to a better correlation of the experimentally observed and simulated structural response. From the theoretical point of view it should be remarked that both the FOSD and the MTSD theory exhibit the well known local equilibrium inconsistency: both do not satisfy the equilibrium of the individual layers.

4. Finite element approach

Eq. (24) forms the basis for the numerical solution by the finite element method. Representing the displacement field of an element as

$$\boldsymbol{v} = \boldsymbol{N}\boldsymbol{q}, \tag{36}$$

where $\boldsymbol{N}$ denotes the matrix of shape functions, and $\boldsymbol{q}$ is the vector of nodal displacements and rotations, Eq. (24) yields

$$(\boldsymbol{Q}^{\mathrm{T}} + (\boldsymbol{C}\dot{\boldsymbol{q}})^{\mathrm{T}} + (\boldsymbol{M}\ddot{\boldsymbol{q}})^{\mathrm{T}} - \boldsymbol{R}^{\mathrm{T}})\delta\boldsymbol{q} = \boldsymbol{0}. \tag{37}$$

Here $\boldsymbol{Q}$ and $\boldsymbol{R}$ are the vectors of balanced and external forces, while $\boldsymbol{M}$ and $\boldsymbol{C}$ are the mass and damping matrices, respectively, which can be found in Palmerio et al. (1990) and Kłosowski and Schmidt (1993, 1996). After an aggregation of all elements, Eq. (37) yields the equations of motion in the form

$$\boldsymbol{M}\ddot{\boldsymbol{q}} + \boldsymbol{C}\dot{\boldsymbol{q}} + \boldsymbol{Q} = \boldsymbol{R}, \tag{38}$$

where $\boldsymbol{M}$, $\boldsymbol{C}$, $\boldsymbol{Q}$ and $\boldsymbol{R}$ denote the respective global matrices and vectors. In the present paper the central difference method is used for the time integration of Eq. (38).

Fig. 2 shows the finite element mesh for a quarter of the plate used in the shock tube experiments. A discretization by 72 nine node isoparametric elements with selective reduced integration was required to

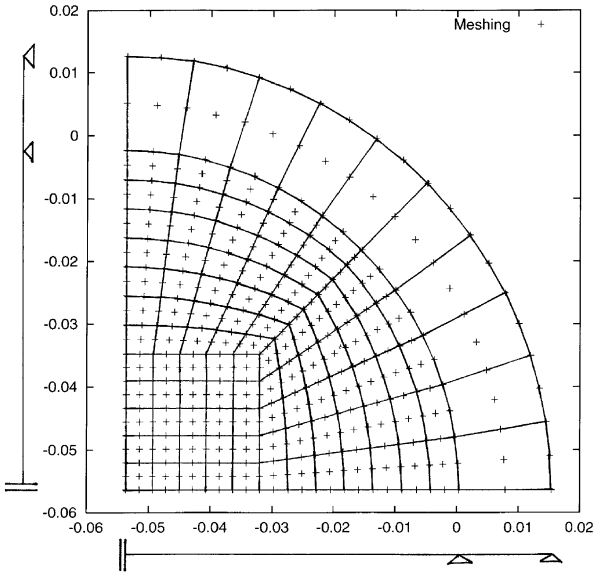

Fig. 2. Finite element mesh of the plate.

achieve a convergent solution. The outer ring represents the clamped area of the plate. The finite element modeling of the clamping conditions is performed on the basis of experimental results for elastic plate vibrations (see Section 7).

5. Experimental setup

For the experimental study of viscoplastic plate vibrations a shock tube is used, see Fig. 3, which consists of a high-pressure chamber (1) and a low-pressure chamber (3), separated from each other by a hostaphane diaphragm (2). At the end of the tube a steel plate with thickness 2 mm and diameter 138 mm is clamped between two ring flanges (4). Because of the clamping, an area of only 108 mm diameter is subjected to shock waves.

In the experiments gas is filled into the high-pressure chamber (1) until the membrane (2) is ruptured. A shock wave travels through the low-pressure chamber (3) and impinges on the plate specimen (4) at the end yielding a high-pressure and high-density pulse. The history of pressure on the plate is measured by piezoelectric sensors suitable for fast changes of pressure. They are located in front of the plate in a separate ring flange. To record the vibrations of the plate a capacitor is used, one plate is the circular front plate of the measurement device and the other one is the plate specimen. Its vibration results in a change of the voltage applied to the capacitor. A calibration curve relating the measured voltage and the distance between the capacitor plates has to be determined. The temperature dependence of the capacitors requires the calibration before each new experiment. In the present study the middle point displacement was recorded.

In order to vary impact period, magnitude, and shape of the pressure evolution, several modifications of the experimental setup are investigated. Their utility is shown in Section 7 and the method is described in the following. In order to control the impulse the high-pressure part is filled with different gases: nitrogen and helium. The lighter the gas, the faster the shock wave and the greater the pressure between shock wave and the steel plate. Furthermore the lighter the gas, the shorter the shock period, which can also be decreased by shortening the high-pressure chamber. The reason for this is as follows: when the membrane breaks a shock wave moves into the low-pressure chamber, besides an expansion wave is generated traveling first into the high-pressure chamber. It is reflected at its end and reaches finally the steel plate, thus destroying the high-pressure state due to the shock wave. This effect is accentuated by choosing a light gas and a short high-pressure chamber.

6. Identification of material parameters

Fig. 4 shows the results of tension tests at seven different strain rates. Applied to the uniaxial tension test the Chaboche law reads:

$$\sigma = k + X + K\dot{\epsilon}_p^{1/n}, \qquad X = \frac{a}{c} - \frac{a}{c}\mathrm{e}^{-c\epsilon^p}. \tag{39}$$

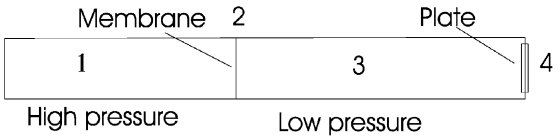

Fig. 3. Principle of the shock tube.

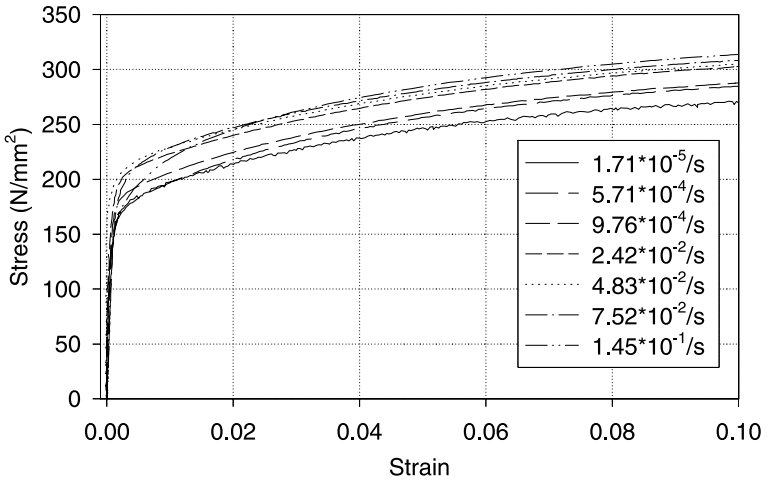

Fig. 4. Tension tests.

Since only tension tests could be performed with the thin steel specimens, a separation of isotropic and kinematic hardening was not possible. Therefore in Eq. (39) pure kinematic hardening is assumed. By means of the quasi-static tension test the yield limit k, the Young's modulus E and the hardening parameters a, c are obtained by curve fitting. The viscous parameters K, n are determined by curve fitting of the overstress versus strain rate relation. Detailed information concerning the identification procedure can be found in (Lemaitre et al., 1994). In this way the following parameters are found:

$$E = 198.6 \times 10^3 \text{ MPa}, \quad a = 2.5 \times 10^3 \text{ MPa}, \quad c = 20.3, \quad k = 167.88 \text{ MPa}, \quad K = 63.12 \text{ MPa}, \quad n = 4.22.$$

The purpose of the extended form of the Chaboche model is to account for the saturation process of the overstress at high strain rates. The method of parameter identification, suggested in Lemaitre and Chaboche (1994) for the classical version of the Chaboche model, is extended here for this refined model. An equivalent viscous exponent N, which controls the saturation process as a function of the overstress, is defined as (see Chaboche, 1989):

$$N = \frac{\mathrm{d} \ln \dot{p}}{\mathrm{d}\sigma_v} = f(\sigma_v) = n + \alpha(n+1)\left(\frac{\sigma_v}{K}\right)^{n+1}. \tag{40}$$

To identify the material parameter α, first a relation between the viscous exponent N and the overstress σ_v must be obtained. This is carried out by curve fitting of the overstress–strain rate relation in five different ranges of the strain rate, see Fig. 5. Starting with a set of three measured points (set 1) in each subsequent set one additional measured point is included. The obtained relation is shown in Table 1.

By describing this new relation with Eq. (40), the parameter α can be determined (see Fig. 6). However, from Eq. (40) it can be seen that only the viscous parameter N is a function of the strain rate, while the second viscous parameter K remains constant for numerical simulations using this model. Since K depends on the strain rates as shown in Table 1, any choice of a particular value restricts the accuracy of the simulation to a special interval of strain rates. The disadvantage of this procedure is shown in Fig. 7, where K is chosen for high strain rates. As a result the calculation of the viscous behavior predicted by using the data set 1 is no more in agreement with the measurement even at low strain rates. Likewise, if K is chosen

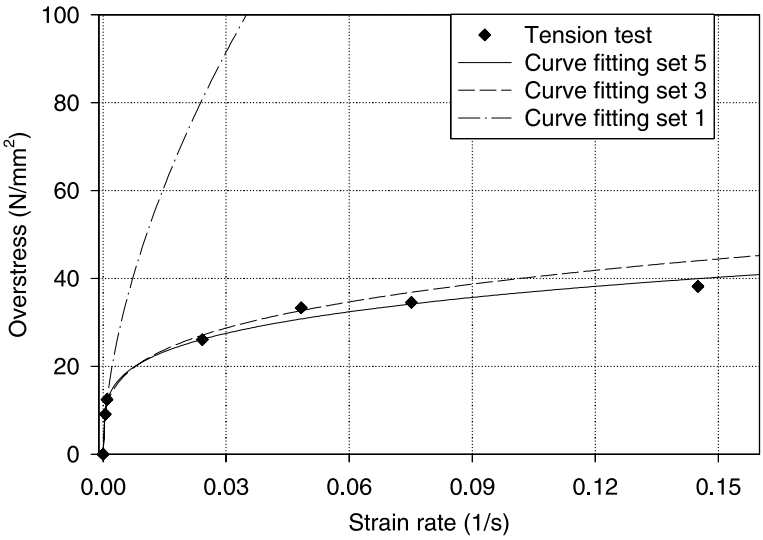

Fig. 5. Curve fittings at different strain rates.

Table 1
Identification of material parameters (extended Chaboche model)

Set	$\dot{\varepsilon}^p$ (1/s)	Overstress (N/mm^2)	K (N/mm^2)	N
1	9.76×10^{-4}	12.42	703.14	1.72
2	2.42×10^{-2}	26.06	67.71	3.91
3	4.83×10^{-2}	33.33	74.44	3.68
4	7.52×10^{-2}	34.54	69.40	3.87
5	1.45×10^{-1}	38.18	63.12	4.22

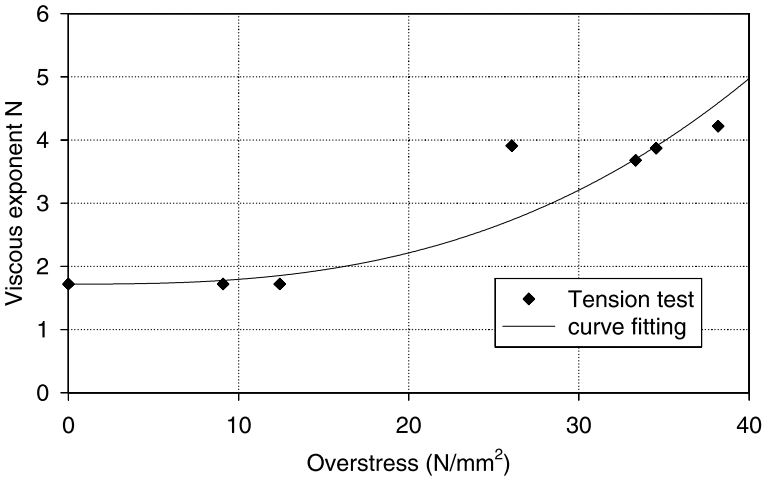

Fig. 6. Relation between viscous exponent N and overstress, describing a saturation of the overstress.

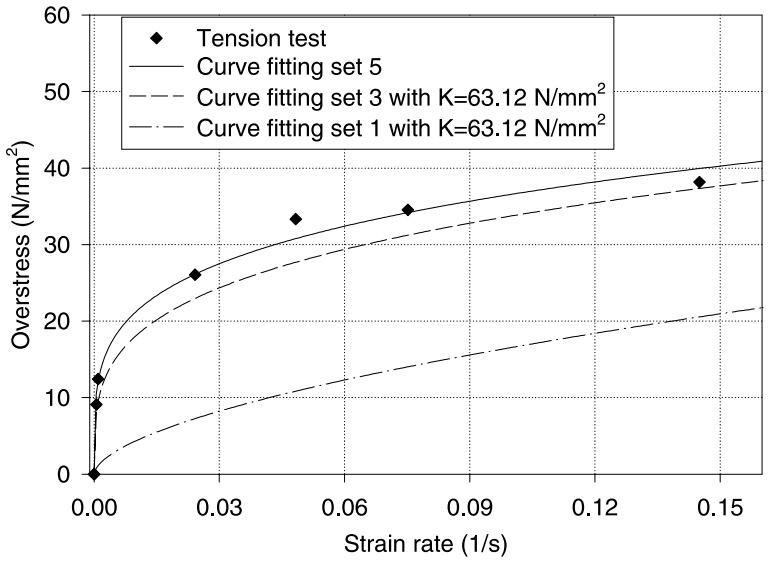

Fig. 7. Effect of the choice of a particular value for the viscous parameter K.

out of a range of low strain rates the accuracy of the calculated high strain rate response would be insufficient.

As a result of the missing separation of elastic, plastic and viscous part in the Bodner–Partom model, the identification of the material parameters m_1, m_2, R_1, D_1, D_0, n, R_0 is complicated. The analytical method applied in the present study was developed in Lindholm et al. (1985) and Chan et al. (1988). Like in the identification on the basis of the Chaboche model only one type of hardening is assumed. Because of the assumed initial isotropic hardening R_0, here the entire hardening is treated as isotropic. In this way the following parameters are obtained:

$$R_0 = 431.86 \text{ MPa}, \quad R_1 = 665.94 \text{ MPa}, \quad m_1 = 0.1214 \text{ (MPa)}^{-1}, \quad D_0 = 1000 \frac{1}{\text{s}}, \quad n = 1.63.$$

7. Experimental and numerical results

7.1. Modeling of boundary conditions and damping

For the simulation, the correct modeling of the boundary conditions is essential. In Section 5 a 'clamping' device was described, however it is not possible to realize ideal clamping. To model the real stiffness of the clamping device, first elastic vibrations are carried out, knowing that the frequency of the vibrations depends on the boundary stiffness. By comparing the experimentally determined frequency of the plate vibrations with FE-simulations it was found that the real clamping conditions can be modeled by an outer ring with Young's modulus 255 000 N/mm^2 (see also Fig. 2).

In order to include an appropriate description of the damping of the vibration it is taken into account that the increasing air density inside the tube causes a greater damping than the air outside. The density between the reflected shock wave and the plate is calculated, based on gas dynamics considerations which can be found in Fieweger (1996). With the obtained density inside and the normal air density outside the tube a ratio between the two damping properties is determined. Then, by adapting the slope of the

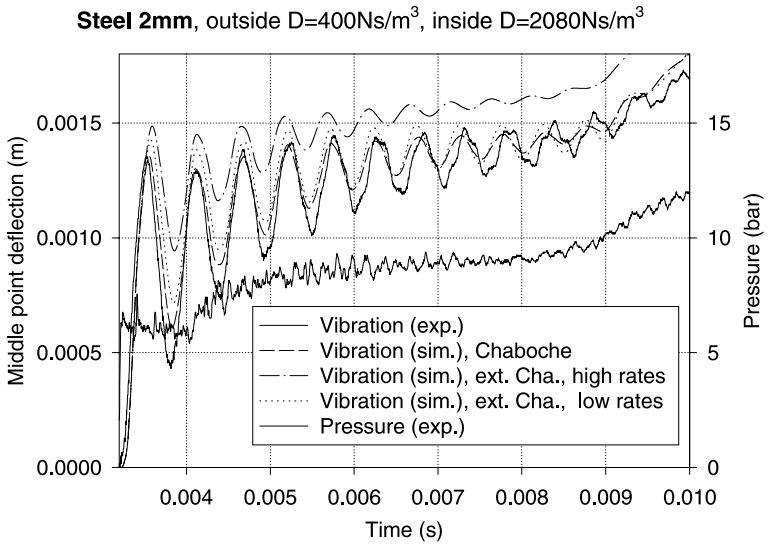

Fig. 8. Comparison between measured and simulated viscoplastic vibrations (Chaboche model).

amplitudes of simulated elastic vibrations to measured ones, the internal and external damping coefficients are determined. Evidently the internal damping is not constant due to the movement of the shock wave in the tube. Nevertheless, the applied method is estimated appropriate to account for an average damping coefficient. For each experiment labels for the internal and external damping coefficients used for numerical simulation are given at the top of the respective diagram.

7.2. Correlation of experimental and predicted vibrations

In Fig. 8, viscoplastic vibrations are presented. It can be seen that the simulations with the classical Chaboche model fit most correctly to the measured vibrations. For the calculations with the extended form of the Chaboche model two possibilities are shown, for low and high strain rates, depending on the value of the viscous parameter K as described in Section 2. The result is that none of them improves the simulation because they involve a restriction to a special interval of strain rates as shown in Section 2, but in a vibrating state of deformation the entire range of strain rates is of the same importance. The simulations using the Bodner–Partom model show very similar vibrations compared to those obtained on the basis of the classical Chaboche model and predict the plate response also well. A greater difference between vibrations calculated by the Chaboche and the Bodner–Partom models was observed in Kłosowski et al. (1995a,b), but there no comparison to an experiment was available to decide which simulation is the better one. In the present paper it is shown that not only both simulations are in good agreement with the experiment, but also the simulations by using the models of Chaboche and Bodner–Partom are very similar to each other.

7.3. Geometrical nonlinearity

Fig. 9 shows numerical results for the rate of the plastic strain tensor invariant versus time at the boundary in some of the ten layers used for through-the-thickness discretization of the plate (see Fig. 1). It can be observed that in the lower layer, 1, yield initiation occurs earlier than in the upper layer, 10. Also, it can be seen that the plastic strain rates in the lower layer are much higher than in the upper one. The same

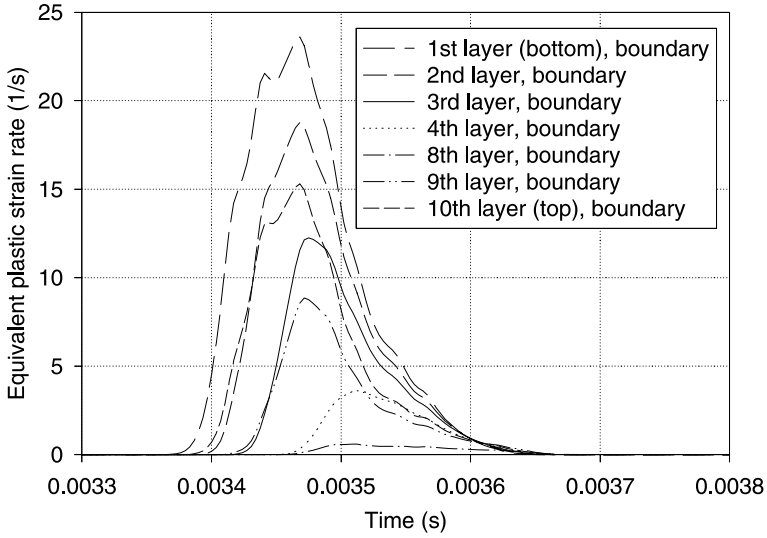

Fig. 9. Rate of the plastic strain tensor invariant versus time at the boundary.

effects, however even more pronounced, can be observed when the layers 3 and 8 are considered, which are located symmetrically to each other in the middle of the lower and upper half, respectively, of the cross section. Plastification in layer 3 starts earlier and is much more intensive than in layer 8, where the plastic strain rates remain very small during the entire impulse duration. These observations show that before yield initiation the plate had reached already a geometrically nonlinear state of deformation in which in addition to the bending moments tensile forces due to large displacements had developed resulting in an asymmetric through-the-thickness distribution of the longitudinal stresses and, subsequently, in a shift of the neutral axis. This result clearly demonstrates that the plate response and in particular phenomena like yield initiation and spread of plastic zones can be accurately predicted only by a geometrically nonlinear theory incorporating both bending and membrane effects. Fig. 10 shows the same effects as Fig. 9, however at the center of the plate. As expected, here the situation is reversed, i.e. in the upper layers, 10 and 9, yield initiation occurs earlier and is accompanied by higher strain rates than in the lower layers, 1 and 2, respectively. This is due to the fact that already in the elastic range the tensile stresses due to bending in the upper layers are increased while the compressive stresses in the lower layers are decreased by tensile forces in the plate due to large deflections. In the analyzed case this geometrically nonlinear effect causes plastification only in layers 1 and 2 of the lower half but in all layers of the upper half of the cross section.

7.4. Modified transverse shear stress distribution

Experimental results were compared to the simulation using the Chaboche model with and without the MTSD described in Section 3 (see Fig. 1), respectively. The simulation turns out to be sensitive to this modification and a better approximation of the experimental results is reached at the lower peaks of the amplitudes. The same holds if the Bodner–Partom model is used.

Fig. 11 shows the effect of the refined transverse shear stress distribution on the prediction of yield initiation through the thickness at the plate boundary. From the plots of the rate of the plastic strain tensor versus time it can be seen that a MTSD based analysis predicts later yield initiation and much smaller plastic strain rates in both the upper and lower layers, 10 and 1, than an analysis based on the transverse shear stress distribution resulting from the FOSD hypothesis. This is due to the fact that in a MTSD based

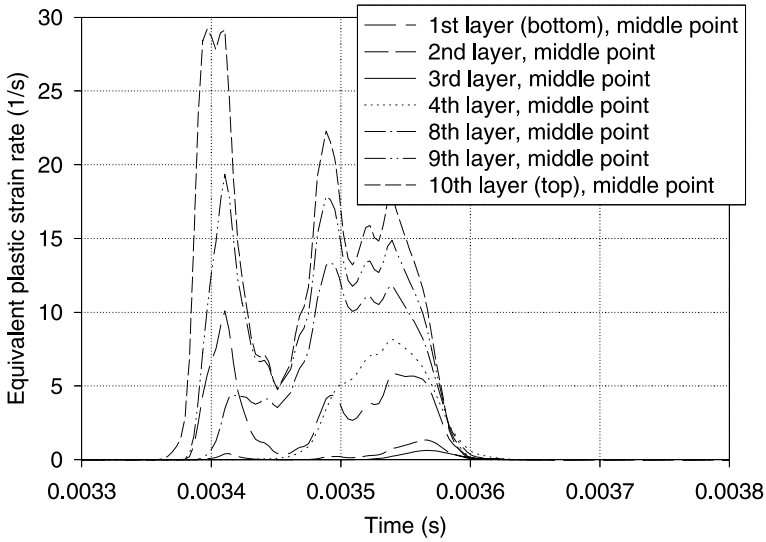

Fig. 10. Rate of the plastic strain tensor invariant versus time at the plate center.

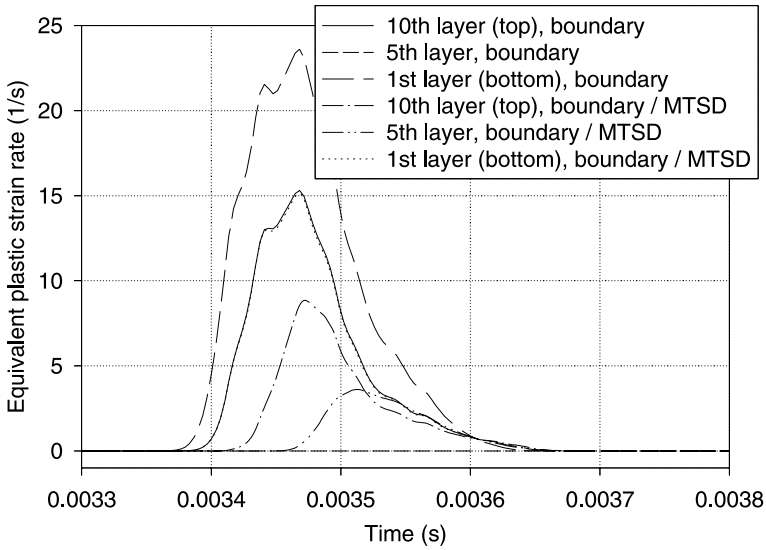

Fig. 11. Rate of the plastic strain tensor invariant versus time at the boundary predicted by FOSD and MTSD analysis.

analysis the transverse shear stresses at the upper and lower surface are zero, hence matching the physical reality, while pure FOSD analysis overestimates these stresses and, subsequently, yield initiation and plastic strain rates in the outer layers. At the midsurface of the plate the situation is reversed, because there the transverse shear stresses of the MTSD model are 50% higher than those of the FOSD theory. The effect is demonstrated in Fig. 12 by the plot corresponding to layer 5 located close to the plate midsurface. While no yield initiation is predicted in this layer by using pure FOSD theory, a MTSD based analysis reveals that plastification indeed occurs.

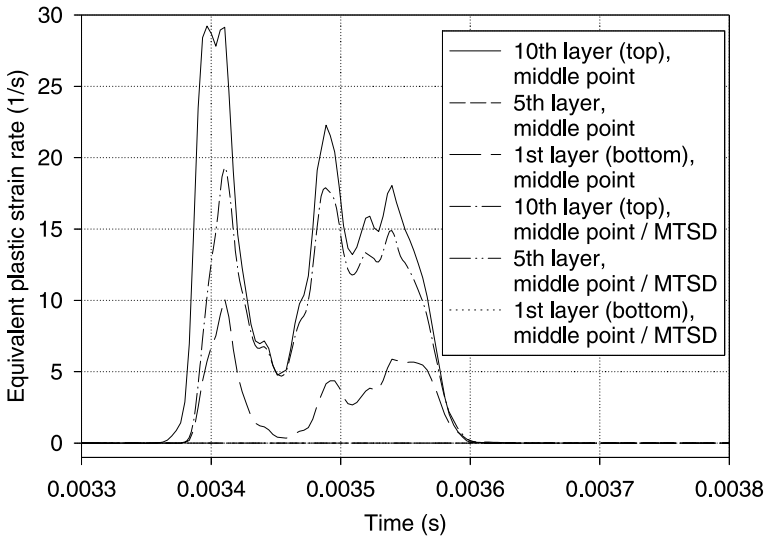

Fig. 12. Rate of the plastic strain tensor invariant versus time at the plate center predicted by FOSD and MTSD analysis.

7.5. Sensitivity of the simulation

Next the sensitivity of the simulated vibrations to variations of the experimentally determined material parameters is studied. In Fig. 13 the experimental results are plotted in comparison to the simulation using the Chaboche model, including the transverse shear stress modification, and another simulation with slightly varying material parameters. The variations of the parameters were generated by omitting in the identification procedure the two uniaxial tension tests at the highest strain rates (see Fig. 4). Using this reduced set of experimental data a new identification of the viscous parameters was carried out in order to

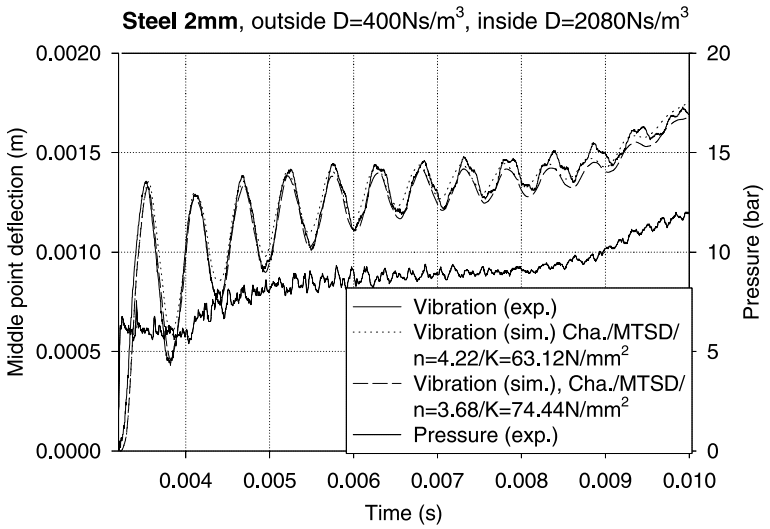

Fig. 13. Sensitivity of the plate response to variations of the material parameters of the Chaboche model.

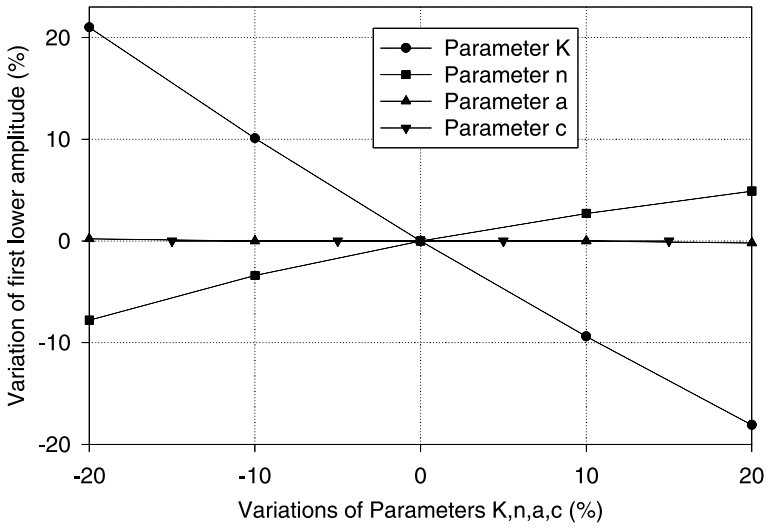

Fig. 14. Material parameter variation for the Chaboche model.

obtain a realistic variation of the material properties. A strong dependence of the lower amplitudes on the viscous parameters is visible in Fig. 13. In order to study the problem of sensitivity more systematically each parameter is varied and new simulations are carried out, taking the change of the first lower amplitude as sensitivity indicator. The results of this procedure are shown in Fig. 14. One sees a strong dependence of the first lower amplitude on the viscous parameters, whereas the result is not sensitive to variations of the hardening parameters. In Figs. 15 and 16 the same study is carried out using the Bodner–Partom model. Again in the identification procedure the two uniaxial tension tests at the highest strain rates were omitted.

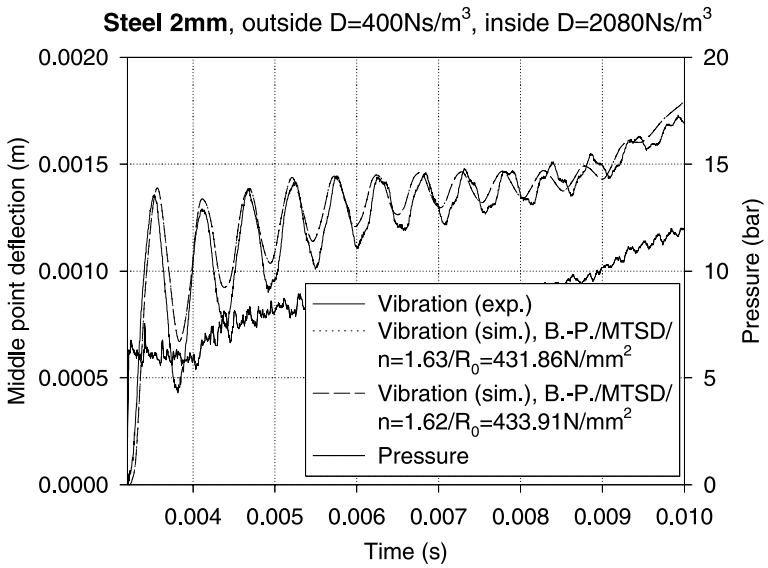

Fig. 15. Sensitivity of the plate response to variation of the material parameters of the Bodner–Partom model.

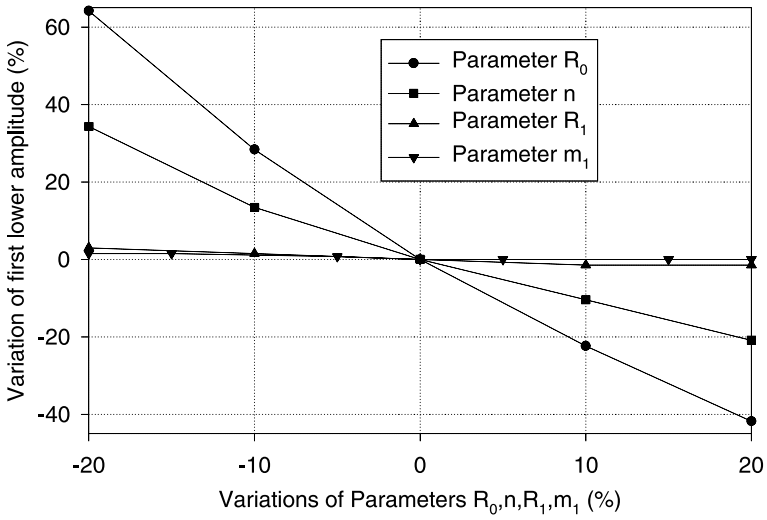

Fig. 16. Material parameter variation for the Bodner–Partom model.

With the new obtained viscous parameters n, R_0 a second simulation is carried out which is also shown in Fig. 15. However, here the change of the material parameters is so small that the two simulations of the plate response are identical. One can see that the identification of the material parameters in the framework of the Bodner–Partom model is much less affected by unavoidable error margins of experimental measurements. Consequently, the numerical simulations of the plate response based on the Bodner–Partom model show considerable less sensitivity to deviations of experimental results in the tension tests than those based on the Chaboche model. The variation of each parameter separately is shown in Fig. 16. Here, a much higher change of the first lower amplitude is observed by varying the viscous parameters by the same percentage as in the Chaboche model. We note that this high sensitivity to material parameter variations does not necessarily cause a high inaccuracy of structural simulations using the Bodner–Partom model. One should keep in mind that variations of the material parameters in the identification procedure are much smaller for the Bodner–Partom model than for the Chaboche model. Thus the fact that Fig. 16 shows a high change of the system response caused by relatively small change of parameters is in agreement with the observation that, vice versa, relatively large error margins in the tension tests cause only small changes of the material parameters in the identification process. Therefore the accuracy of a viscoplastic model cannot be estimated exclusively by the sensitivity to material parameter variation. It is as important to take into account the variation of parameters induced by error margins in tension tests. Only the superposition of both effects can lead to an objective statement about the accuracy of the used model. In this sense the Bodner–Partom model has been shown to be more stable than the Chaboche model (see Figs. 13 and 15) for the studied problem.

7.6. Various time histories

Measured and simulated vibrations at higher pressures and larger displacements were considered. In Fig. 17, the maximum rotations in the plate versus time are plotted for a pressure history with the highest peak pressure used in the experiments. It can be seen that the observed plate deformations do not violate the used shell theory concerning the assumption of moderate rotations.

To check if the good correlation between experiment and simulation are not accidental the pressure impulses were changed by modifying the shock tube as described in Section 5. So, instead of nitrogen and a

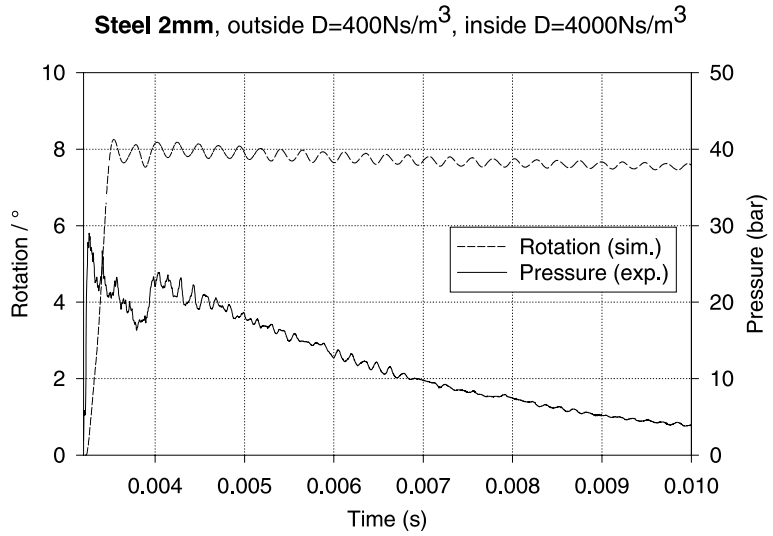

Fig. 17. Maximum rotations at the midsurface.

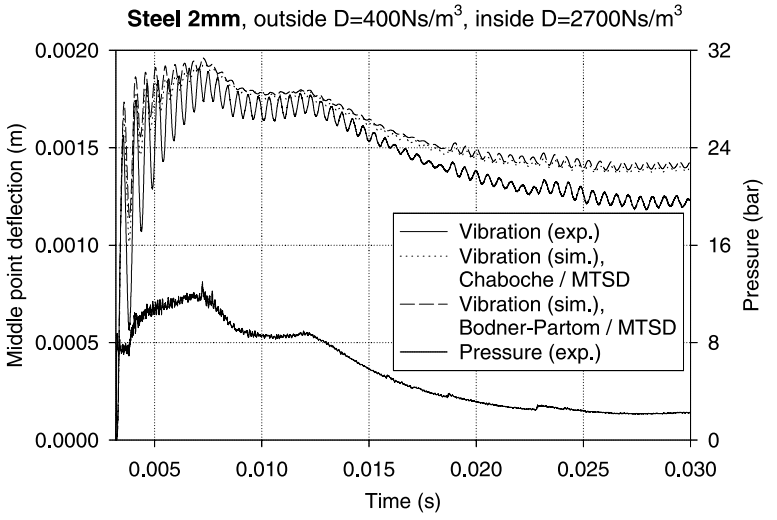

Fig. 18. Experiment using helium and a long high-pressure chamber.

long high-pressure chamber used in Figs. 8, 13 and 15, in the experiments presented in Fig. 17 helium with a short high-pressure chamber and in Fig. 18 helium with a long high-pressure chamber are used. It can be observed that also in these experiments with very different impact periods, magnitudes, and shapes of the pressure evolution a good correlation of measured and simulated plate response is achieved.

8. Conclusions

In the present paper the transient large amplitude oscillations of steel plates subjected to shock waves was studied experimentally and numerically. Calculations were carried out by nonlinear finite element

analysis based on a layered model including the effects of transverse shear and rotary inertia. Parameter identifications by means of uniaxial tension tests were performed for the Chaboche and Bodner–Partom viscoplastic constitutive laws. Based on these identifications a good correlation of the predicted and experimental inelastic dynamic response and permanent deflections was achieved with both models. An analysis of the sensitivity of the predicted response to variations of the material parameters revealed that the simulations based on the Bodner–Partom model show considerable less sensitivity to deviations of the experimental results in uniaxial tension tests, because the result of the identification is much less affected than in the case of the Chaboche model. Comparative analysis using a refined transverse shear stress distribution to trace the evolution of the material behavior showed a significant effect on the prediction of yield initiation and plastic strain propagation and led to a better correlation of the experimental and simulated transient responses.

Acknowledgements

The uniaxial tension tests for the identification of material parameters for the considered constitutive equations have been carried out by Prof. E. El-Magd, Lehr- und Forschungsgebiet Werkstoffkunde, RWTH Aachen, to whom the authors would like to express their grateful thanks.

References

Batra, R.C., Dubey, R.N., 1971. Impulsively loaded circular plates. Int. J. Solids Struct. 7, 965–978.

Bodner, S.R., Partom, Y., 1975. Constitutive equations for elasto-viscoplastic strain-hardening materials. ASME J. Appl. Mech., 385–389.

Bodner, S.R., Symonds, P.S., 1979. Experiments on viscoplastic response of circular plates to impulsive loading. J. Mech. Phys. Solids 27, 91–113.

Chaboche, J.L., 1989. Constitutive equations for cyclic plasticity and cyclic viscoplasticity. Int. J. Plast. 5, 247–302.

Chan, K.S., Bodner, S.R., Lindholm, U.S., 1988. Phenomenological modeling of hardening and thermal recovery in metals. J. Eng. Mat. Tech. 110, 1–8.

Chroscielewski, J., Kłosowski, P., Pfahl, U., Schmidt, R., Weichert, D., Plates and shells under impact loading. Proc of the Int Symp on Dynamics of Continua, Bad Honnef, in press.

Fieweger, K., 1996. Selbstzündung von Kohlenwasserstoff/Luft-Gemischen unter motorischen Randbedingungen. RWTH Aachen.

Florence, A.L., Firth, R.D., 1965. Rigid-plastic beams under uniformly distributed impulses. ASME J. Appl. Mech. 32, 481–488.

Florence, A.L., 1966. Circular plate under a uniformly distributed impulse. Int. J. Solids Struct. 2, 37–47.

Gerard, G., 1956. A new experimental technique for applying impulse loads. Proc. Symp. on Impact Testing, Atlantic City, N.Y. 1955, ASTM Special Technical Publications 176, 94–109.

Idczak, W., Rymarz, Cz., Spychala, A., 1980. Large deflection of a rigid-viscoplastic impulsively loaded circular plate. J. Tech. Phys. 21, 473–487.

Idczak, W., Rymarz, Cz., Spychała, A., 1981. Studies on shock-wave loaded, clamped circular plates. J. Tech. Phys. 22, 175–184.

Jones, N., Walters, R.M., 1972. A comparison of theory and experiments on the dynamic plastic behavior of shells. Archives of Mechanics 24, 701–714.

Jones, N., 1989. Structural Impact. Cambridge University Press.

Kłosowski, P., Schmidt, R., 1993. Geometrically nonlinear transient analysis of laminated composite plates. ZAMM 73 (7/8), T903–T906.

Kłosowski, P., Schmidt, R., 1994. Large amplitude oscillations of laminated composite shells under time-dependent loading. ZAMM 74, T138–T140.

Kłosowski, P., Woznica, K., Weichert, D., 1995a. A comparative study of vibrations of elasto-viscoplastic shells and plates. Engng. Trans. 43 (1–2), 183–204.

Kłosowski, P., Woznica, K., Weichert, D., 1995b. Dynamics of elasto-viscoplastic plates and shells. Archive Appl. Mech. 65, 326–345.

Kłosowski, P., Schmidt, R., 1996. Geometrically and physically nonlinear transient analysis of structures. In: Bogacz, R., Ostermeyer, G.P., Popp, K. (Eds.), Dynamical Problems in Mechanical Systems, IV, Polish Academy of Sciences, Warsaw, pp. 171–182.

Kłosowski, P., 1999. Nonlinear numerical analysis and experimental investigation of the elasto-plastic behavior of plates and shells. Thesis, Politechnica Gdanska (in Polish).

Kłosowski, P., Woznica, K., Weichert, D., 2000. Comparison of numerical modeling and experiments for dynamic response of circular elasto-viscoplastic plates. European J. Mech., A/Solids 19, 343–359.

Kreja, I., Schmidt, R., 1995. Moderate rotation shell theory in FEM application, Scientific Publications of the Technical University of Gdansk 522, 229–249.

Kreja, I., Schmidt, R., Reddy, J.N., 1997. Finite elements based on a first-order shear deformation moderate rotation shell theory with applications to the analysis of composite structures. Int. J. Non-Linear Mech. 32, 1123–1142.

Leech, J.W., Witmer, E.A., Pian, T.H.H., 1968. Numerical calculation technique for large elastic–plastic transient deformations of thin shells. AIAA J. 6, 2352–2359.

Lemaitre, J., Chaboche, J.L., 1994. Mechanics of Solid Materials. Cambridge University Press.

Librescu, Schmidt, R., 1988. Refined theories of elastic anisotropic shells accounting for small strains and moderate rotations. Int. J. Non-Linear Mech. 23, 217–229.

Lindholm, U.S., Chan, K.S., Bodner, S.R., Weber, R.M., Walker, K.P., Cassenti, B.N., 1985. Constitutive modeling for isotropic materials.(HOST), Second Annual Status Report, NASA-CR 174980, Contract no. NAS3-23925.

Palmerio, A.F., Reddy, J.N., Schmidt, R., 1990. On a moderate rotation theory of laminated anisotropic shells – Part 1. Theory, Part 2. Finite Element Analysis. Int. J. Non-Linear Mech. 25, 687–714.

Pennetier, O., 1998. Interaction Structures-Detonations, Atténuation des efforts retransmis et étude de la réponse dynamique non linéaire de voiles minces. Thesis, Université d'Orléans.

Renard, J., Pennetier, O., 1996. Nonlinear dynamic response of plates submitted to an explosion-numerical and experimental study. Structural Dynamics-EURODYN'96, Balkema, Rotterdam, pp. 689–694.

Schmidt, R., Reddy, J.N., 1988. A refined small strain moderate rotation theory of elastic anisotropic shells. ASME J. Appl. Mech. 55, 611–617.

Schmidt, R., Weichert, D., 1989. A refined theory of elastic–plastic shells at moderate rotations. ZAMM 69, 11–21.

Stoffel, M., Schmidt, R., Weichert, D., 1998. Vibrations of viscoplastic plates under impact load. In: Jones, N., Talaslidis, D.G., Brebbia, C.A., Manolis, G.D. (Eds.), Structures under Shock and Impact V, Computational Mechanics Publications, Southampton-Boston, pp. 299–308.

Stoffel, M., Weichert, D., 1999. Anwendungsgrenzen viskoplastischer Stoffgesetze bei Plattenschwingungen. Proc. of GAMM 98, ZAMM, 79, 2, pp. S321–S322.

Stoffel, M., Schmidt, R., Weichert, D., 1999. Limit states of deformations of shock wave loaded viscoplastic structures. In: Chen, C.S., Brebbia, C.A., Pepper, D.W., Harik, I., (Eds.), Boundary Element Technology inc. Computational Methods and Testing for Engineering Integrity, WIT Press, Southampton-Boston, pp. 629–638.

Stoffel, M., Schmidt, R., Weichert, D., 2000. Pseudo-Shakedown viskoplastischer Flächentragwerke. Proc. of GAMM 99, ZAMM, 80, pp. S303–S304.

Stronge, W.J., Yu, T.X., 1993. Dynamic Models for Structural Plasticity. Springer, Berlin.

Wang, A.J., 1955. The permanent deflection of a plastic plate under blast loading. J. Appl. Mech. 22, 375.

Weichert, D., Stoffel, M., 1998. Theoretical and experimental investigations on plates under impulsive loading. In: Theocaris, P.S., Fotiadis, D.I., Massalas, C.V. (Eds.), Proceedings of the Fifth National Congress on Mechanics, 1 University of Ioannina Press, Ioannina, pp. 72–83.

Wierzbicki, T., Florence, A.L., 1970. A theoretical and experimental investigation of impulsively loaded clamped circular viscoplastic plates. Int. J. Solids Struct. 6, 553–568.

Witmer, E.A., Balmer, H.A., Leech, J.W., Pian, T.H.H., 1963. Large dynamic deformations of beams, rings, plates, and shells. AIAA J. 1, 1848–1857.

Woznica, K., 1996. Models of elasto-viscoplastic behaviour of structures under dynamic load. Mécanique Industrielle et Matériaux 49, 75–78.

Woznica, K., Kłosowski, P., 1997. Constitutive laws of viscoplasticity in dynamic response of structures. Engng. Trans. 45, 1.

Woznica, K., 1997. Dynamique des structures elasto-viscoplastiques. Thesis, Laboratoire de Mécanique de Lille.

Woznica, K., 1998. Dynamic behaviour of the elasto-viscoplastic structures – material parameter identification problems for different constitutive laws. Mécanique Industrielle et Matériaux 51, 103–105.